RESEARCH ARTICLE

CARBON ENERGY WILEY

Practical operating flexibility of a bifunctional freestanding membrane for efficient anion exchange membrane water electrolysis across all current ranges

Hong-Jin Son[1] | **Jeemin Hwang[2,3]** | **Min Young Choi[4]** | **Seung Hee Park[1]** | **Jae Hyuk Jang[4]** | **Byungchan Han[3]** | **Sung Hoon Ahn[1]** 🟢

[1]Department of Bio-Chemical Engineering, Chosun University, Gwangju, Republic of Korea

[2]Fuel Cell Research and Demonstration Center, Hydrogen Energy Research Division, Korea Institute of Energy Research (KIER), Buan-gun, Jeollabuk-do, Republic of Korea

[3]Department of Chemical and Biomolecular Engineering, Yonsei University, Seoul, Republic of Korea

[4]Center for Research Equipment, Korea Basic Science Institute, Daejeon, Republic of Korea

Correspondence
Sung Hoon Ahn, Department of Bio-Chemical Engineering, Chosun University, 309 Pilmun-daero, Dong-gu 61452, Gwangju, Republic of Korea.
Email: sunghoon@chosun.ac.kr

Abstract
This study explores a symmetric configuration approach in anion exchange membrane (AEM) water electrolysis, focusing on overcoming adaptability challenges in dynamic conditions. Here, a rapid and mild synthesis technique for fabricating fibrous membrane-type catalyst electrodes is developed. Our method leverages the contrasting oxidation states between the sulfur-doped $NiFe(OH)_2$ shell and the metallic Ni core, as revealed by electron energy loss spectroscopy. Theoretical evaluations confirm that the $S–NiFe(OH)_2$ active sites optimize free energy for alkaline water electrolysis intermediates. This technique bypasses traditional energy-intensive processes, achieving superior bifunctional activity beyond current benchmarks. The symmetric AEM water electrolyzer demonstrates a current density of $2\,A\,cm^{-2}$ at 1.78 V at 60°C in 1 M KOH electrolyte and also sustains ampere-scale water electrolysis below 2.0 V for 140 h even in ambient conditions. These results highlight the system's operational flexibility and structural stability, marking a significant advancement in AEM water electrolysis technology.

KEYWORDS
AEM water electrolysis, fibrous membrane, iR correction free, operational stability, symmetric configuration

---

1 | INTRODUCTION

As part of the global drive toward carbon neutrality, there are increasing efforts to optimize water electrolysis systems, which are essential for the sustainable production of green hydrogen. Proton exchange membrane electrolysis is highly efficient; however, it requires the significant use of scarce platinum group metals (PGMs), such as platinum for the hydrogen evolution reaction (HER) and iridium for the oxygen evolution reaction (OER). To address this, there have been notable advances in which first-row transition metals have been employed as electrocatalysts, exhibiting comparable or even superior catalytic activity compared to PGM catalysts in alkaline media. Recent developments in alkaline electrolysis with zero-gap configurations using anion exchange membranes (AEMs) have notably shifted the performance landscape, allowing operation at voltages below 2.0 V for ampere-scale hydrogen production.[1–12] Although significant progress has been made, electrodes for industrial-scale water electrolysis still exhibit issues related to practical performance, durability, and operational versatility under dynamic conditions. To achieve ampere-scale hydrogen production, it is essential to consider series resistance, a major factor contributing to energy loss. This resistance comprises ohmic, charge-transfer, and mass-transport components and is increasingly challenging at higher current densities. In ultra-thin-film catalysts, ohmic resistance is generally attributed to solution resistance ($R_{solution}$) and is commonly adjusted by using the iR correction technique to evaluate intrinsic activity. However, in practical electrodes, ohmic resistance is more complex, consisting of both $R_{solution}$ and electrode resistances ($R_{electrode}$).[13] An imprecise iR correction can result in overcompensation, complicating the assessment of the real catalytic performance of the electrode. For example, nickel–iron (NiFe) (oxy)hydroxide catalysts display high intrinsic OER activity but suffer from their low electrical conductivity.[14] Although three-dimensional (3D) nickel foams are commonly used as current collectors to mitigate this issue, they introduce other forms of resistance, such as interfacial and internal electrode resistances. To accurately assess the performance of a practical catalytic electrode, one should either use a more refined iR correction technique or conduct evaluations under iR correction-free conditions.[13,15] Mass transport efficiency is another crucial factor in ampere-scale water electrolysis. For example, gas bubble formation in the micropores of conventional nickel foam can block active sites, thereby compromising overall water splitting (OWS) performance. To address this issue, researchers have suggested the use of low-dimensional fibrous structures[16] or 3D-printed uniform structures[1,17–19] in nickel electrodes as alternatives to nickel foam. These

innovative approaches aim to enhance mass transport efficiency and reduce series resistance, thereby improving the performance of catalyst electrodes. Nonetheless, the fabrication methods for these 3D electrodes can be labor-intensive and energy-consuming, and sometimes pose an explosion risk, especially when a reducing atmosphere containing hydrogen gas is involved.[17,18] Similarly, introducing or generating catalytically active sites, such as metal chalcogenides (M–X, where X can be S, Se, or P)[20–22] or NiMo,[23,24] onto 3D Ni-based substrates also creates challenges in energy efficiency and safety concerns. Therefore, there is a growing interest in developing alternative synthesis methods for practical electrodes that avoid energy-intensive steps. For instance, mild-condition chemical reduction methods have been used to create 1D nanowire arrays.[25] These arrays often feature heterostructures consisting of a conductive metallic core with highly active surface shell layers, thereby improving charge transfer efficiency.

Stability under dynamic operating conditions is a significant concern for industrial water electrolysis. Currently, the most efficient alkaline water electrolysis systems are constructed using an asymmetric electrode configuration.[4,5,10,26–28] This configuration, despite its efficacy, often encounters issues of structural stability, particularly when integrating metal cathodes with metal (oxi)hydroxide anodes. For instance, NiFe (oxy)hydroxides can quickly lose their OER activity under oxidizing conditions with a current density higher than 100 mA cm^{-2} [29–32] or during dynamic on–off cycles.[33] Metallic cathodes also suffer irreversible oxidation under shut-down conditions, leading to permanent loss of their HER activity.[34,35] Employing structurally stable bifunctional electrodes can simplify both the assembly and operation of electrolysis systems. For example, electrodes fabricated using milder methods forego the energy-intensive heat treatments needed to consolidate the separate synthesis steps of conventional HER and OER electrodes. Moreover, the symmetric configuration of bifunctional electrodes in water electrolysis systems shows advantages, with improved long-term structural stability and operating flexibility. The reversibility between HER and OER afforded by bifunctional catalyst electrodes can potentially provide additional benefits.[36–38] Assessing this reversibility can be performed through repeated polarity reversal tests or dynamic on–off cycle tests in symmetrical electrolysis systems.

In this study, we propose a freestanding, fibrous membrane as a practical catalytic electrode in a symmetric AEM water electrolysis system. The substrate-free, fibrous matrices minimize potential increases in resistance from ohmic, charge-transfer, and mass-transport sources,

thereby optimizing ampere-scale hydrogen production. Aligning the nickel network with magnetic fields results in extended nanowires, endowing the fully connected fibrous membrane with robust mechanical properties and flexibility. The two-step synthesis method employs a rapid and cost-effective mild-condition solution process, uniformly introducing sulfur-incorporated $NiFe(OH)_2$ domains onto a refined fibrous nickel matrix. Electron energy loss spectroscopy (EELS) reveals a well-connected conductive core, while the surface is transformed into an oxidized active $S–NiFe(OH)_2$ domain. The constructed image reveals an incremental oxidation state from the core to the surface, which facilitates easier charge transfer within these localized heterostructures. The resulting electrode showed low overpotentials of 25 and 198 mV at current densities of 10 and 1000 mA cm^{-2} for HER and 174 and 270 mV for OER, respectively, outperforming benchmark Pt/C or Ni–Fe hydroxide catalysts. Additionally, it requires only 330 mV for HER and 350 mV for OER at 1 A cm^{-2}, even under iR correction-free conditions. Density-functional theory (DFT) calculations support the superior bifunctional activity and reversibility in both HER and OER due to optimized Gibbs free energy on the $S–NiFe(OH)_2$ lattice. The alkaline water electrolysis system generated a stable current density of 500 mA cm^{-2} at 1.67 V for 150 h, and no significant performance change was observed after switching between HER and OER electrodes. In a symmetric configuration within an AEM water electrolyzer, the bifunctional electrodes exhibited high performance, generating 1 A cm^{-2} at the applied voltage of 1.88 V at room temperature without the need for iR correction. Furthermore, these electrodes demonstrated excellent structural stability during subsequent on–off cycles and reverse polarity tests. This design offers a new pathway for improving the efficiency and stability of existing systems, presenting a practical solution for reversible, ampere-scale bifunctional activity.

2 | EXPERIMENTAL SECTION

2.1 | Synthesis of freestanding membrane-type samples

1 g of nickel(II) chloride hexahydrate ($Ni(NO_3)_2·6H_2O$) and 2 g of sodium hydroxide were dissolved in 200 mL of ethylene glycol under magnetic stirring. Then, a magnetic field was constructed by attaching two pieces of neodymium–iron–boron magnets to the outside of the glass beaker. Afterward, 20 mL of hydrazine monohydrate was added into the solution to induce the directional growth and self-assembly of nickel nanofiber sponge (denoted as $Ni–Ni(OH)_2$) at 70°C for 15 min. The obtained $Ni–Ni(OH)_2$ sponge was washed three times with deionized water and then pressed into a freestanding $Ni–Ni(OH)_2$ membrane. Typically, this membrane is left to air dry overnight to promote the formation of a surface oxidized layer. However, it is worth noting that this drying step can be omitted when preparing the $Ni–S–NiFe(OH)_2$ sample, as the subsequent partial sulfurization process will foster the development of an alternative $S–NiFe(OH)_2$ overlayer. The as-prepared membrane was cut into several $1 × 2$ cm^2 pieces. One piece of $Ni–Ni(OH)_2$ was immersed into 10 mL of aqueous solution containing 0.35 g of iron(III) nitrate nonahydrate ($Fe(NO_3)_3·9H_2O$). Afterward, 0.05 g of sodium thiosulfate pentahydrate was added and reacted at room temperature for 5 min (denoted as $Ni–S–NiFe(OH)_2$).

2.2 | Synthesis of freestanding membrane-type control samples

As a control sample, a $Ni–Ni(OH)_2$ membrane was immersed in a 10 mL aqueous solution containing 0.35 g of $Fe(NO_3)_3·9H_2O$ and allowed to react at room temperature for 12 h. After the reaction, the sample was washed three times with deionized water and dried, resulting in sulfur-free $Ni–NiFe(OH)_2$. Additionally, a high-energy thermal sulfurization process was carried out for the synthesis of fully sulfurized samples. In this process, 0.5 g of sulfur powder and $Ni–Ni(OH)_2$ or $Ni–S–NiFe(OH)_2$ samples were placed in separate alumina crucible boats, about 2 cm apart, inside a quartz tube. The sulfurization was conducted at 350°C for 2 h with a heating rate of 5°C min^{-1} under an argon atmosphere, and the resultant samples were accordingly designated as Ni–NiS and Ni–NiFeS.

2.3 | Synthesis of nickel foam-based control samples

To construct the control samples, commercial nickel foam (110 ppi, 2 mm thickness) with a dimension of $1 × 2$ cm^2 was washed with ethanol, acetone, and deionized water by ultrasonication processes for 30 min each. Then, nickel foam was immersed into 10 mL of aqueous solution containing 0.1 M $Ni(NO_3)_2·6H_2O$ and 0.25 M hexamethylenetetramine and reacted at 95°C for 12 h by the hydrothermal reaction. After cooling down, the obtained sample was washed with deionized water three times and dried to obtain $Ni(OH)_2$. In addition, nickel-foam-based $NiFe(OH)_2$ and $S-NiFe(OH)_2$ were

also prepared by identical processes for Ni–NiFe(OH)$_2$ and Ni–S–NiFe(OH)$_2$. It should be noted that these control samples are distinct from the membrane-type samples, which are identified by an additional "Ni–" prefix in their labels.

2.4 | Synthesis of conventional Pt/C and RuO$_2$ electrodes

RuO$_2$ nanoparticles were synthesized as previously reported in the literature.[30] A solution containing 50 mM ruthenium(III) chloride hydrate was prepared in a 1:1 volume mixture of methanol and water, followed by vigorous magnetic stirring. Sodium hydroxide (2 M) solution was gradually added until a pH of 7 was reached. The resulting material was centrifuged, washed with deionized water, and dried at 60°C before being annealed at 500°C for 5 h in air. For conventional Pt/C or RuO$_2$ electrodes, an ink solution comprising 10 mg of catalyst, 1.95 mL of isopropanol, and 50 µL of 5 wt% Nafion solution was applied to a carbon nanofiber paper at a loading amount of ~4 mg cm^{-2}.

2.5 | Electrochemical analysis

All electrochemical measurements were carried out on a bichannel electrochemical workstation (ZIVE BCP2; WONATECH). The electrochemical properties were evaluated in 1 M KOH electrolyte in a three-electrode system with a graphite rod as a counter electrode and with a Hg/HgO electrode filled with 1 M NaOH solution as a reference electrode. The HER catalytic activity was evaluated by linear sweep voltammetry (LSV) curves at a scan rate of 0.2 mV s^{-1} in 1 M KOH electrolyte with 100% IR correction. The resistance in the high-frequency region (R_{HRF}) value for iR correction was obtained from a Nyquist plot, which was carried out at a current density of -0.1 mA. To prevent the overestimation of OER catalytic activity due to the overlapped redox reaction of the Ni species, cyclic voltammetry (CV) cycles were recorded at a scan rate of 1 mV s^{-1}, and the overpotential values at the specific current densities were obtained from a backward scan of the CV. Electrochemical impedance spectroscopy (EIS) was obtained with the applied overpotential value of 200 mV from 0.1 Hz to 1 MHz with an amplitude of 10 mV. All the potentials in the three-electrode system were converted to the potential versus reversible hydrogen electrode (E_{RHE}), and the reference electrodes were experimentally calibrated in an H$_2$-saturated 1 M KOH electrolyte. The multistep chronopotentiometry curves toward both HER and OER were obtained at various current densities without IR correction. The double-layer capacitance

(C_{dl}) values were calculated from CV curves with various scan rates of 10–100 mV s^{-1}. The OWS performance was evaluated in a two-electrode system with symmetric two membrane-type electrodes or an asymmetric Pt/C cathode coupled with an RuO$_2$ anode. The stability of the catalysts for OWS was tested by the chronopotentiometry test at 100 or 500 mA cm^{-2} in 1 M KOH electrolyte. The symmetric AEM water electrolysis unit was assembled with two Ni–S–NiFe (OH)$_2$ electrodes and a Fumasep FAA-3–50 AEM. The membrane was soaked in KOH for 24 h as an activation treatment before use. With an active area of 1 cm^{-2}, the electrolytic cell was operated in an electrolyte of 1 M KOH at different temperatures. A metering pump maintained a constant electrolyte flow rate of 40 mL min^{-1} from a reservoir to the electrolysis chamber. Chronopotentiometric on–off tests were performed at alternating current densities of 0.4 and 0 A cm^{-2}, each sustained for 5-min intervals. Additionally, polarity reversal experiments were executed at a current density of 0.4 A cm^{-2}, with polarity switching every 30 min over an 18-h period. A detailed analysis of overvoltages was conducted, where the cell voltage (E_{cell}) of the water electrolyzer was understood as the sum of the reversible cell voltage and three distinct overvoltages of kinetic overvoltage (η_{kin}), ohmic overvoltage (η_{Ohm}), and mass transport overvoltage (η_{mass}).[3,68,69] The kinetic cell voltage (E_{kin}) and kinetic overvoltage (η_{kin}) were obtained from Tafel plots. The ohmic overvoltage (η_{ohm}) was obtained by multiplying current density (j) i and R_{HFR}. And then, the mass transport overvoltage (η_{mass}) was determined by subtracting the reversible voltage (E_{rev}), η_{kin}, and η_{ohm} from E_{cell}.

3 | RESULTS AND DISCUSSIONS

3.1 | Preparation of freestanding catalyst membranes and morphological observation

Figure 1 illustrates the two-step, solution-based synthesis process employed to fabricate a freestanding, membrane-type bifunctional catalyst electrode. The first stage involves the self-assembly of a fibrous metallic nickel network, which is achieved through the directional growth of metallic Ni nanoparticles under the guidance of a magnetic field, as indicated by white dotted arrows (Figure S1A,B). This magnetic field is created by two neodymium–iron–boron magnets placed on the outer wall of a glass beaker. The ferromagnetic properties of the nickel nanoparticles align them along these magnetic field lines, facilitating in situ growth and directional alignment. Simultaneously, the resultant fibrous networks intertwine with each other, self-assembling into a freestanding membrane with a 3D,
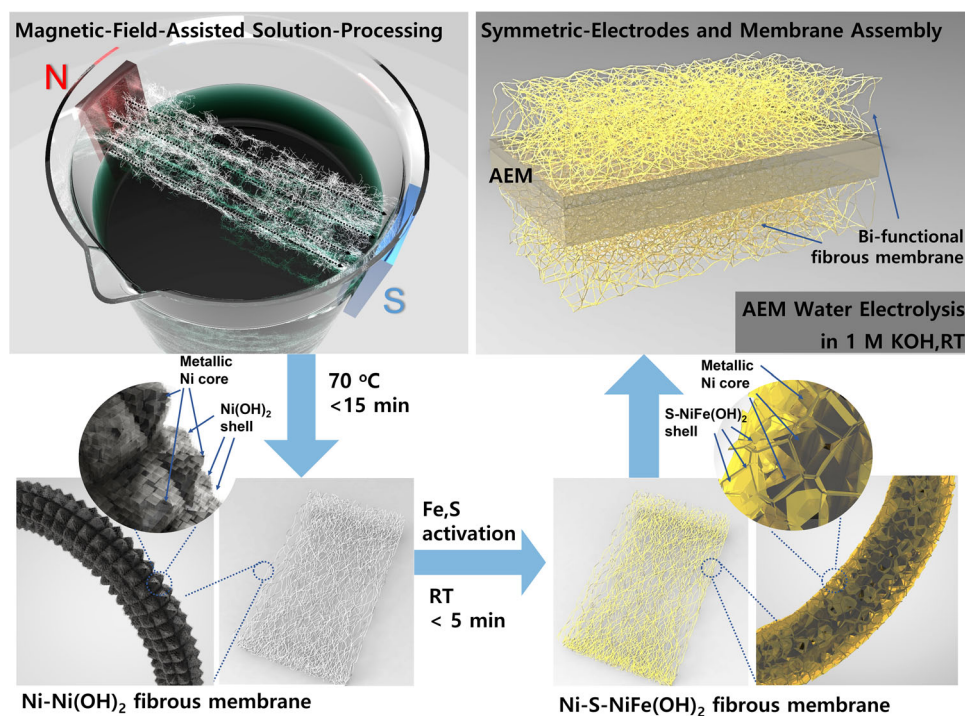
FIGURE 1 Schematic illustration of the synthesis process of the freestanding Ni–S–NiFe(OH)$_2$ membrane under mild conditions.

sponge-like structure. Remarkably, this process does not require any specialized equipment and can be completed in only 15 min at a mild temperature of 70°C. This rapid and mild-condition synthesis process of a fibrous membrane electrode is remarkable, especially compared to the time- and energy-intensive processes for producing commercial nickel foam, which is commonly used as a catalyst electrode. While synthesis processes involving high-temperature sintering promote the full reduction or oxidation of the metal, milder synthesis methods using solution treatment more readily led to the formation of heterostructures composed of metal–metal oxide interfaces. Additionally, in the subsequent process of forming active domains, foam structures with tens of micrometers of pores tend to result in fewer active domains compared to nanofibrous structures. This difference suggests the presence of a larger amount of nonreactive metal substrates, resulting in reduced cost-effectiveness. The size of the fibrous sponge was determined by the diameter of the glass beaker used, typically around 6 cm. Its average weight was ~25 mg cm^{-2}, which is notably lighter than the average weight of nickel foam (~52 mg cm^{-2}), with a density of 110 pores per inch (ppi) and a thickness of 2 mm. The as-prepared sponge could be pressed into a freestanding flexible membrane (Figure S1C) and was easily cut into desired sizes, such as 1 × 2 cm^{-2} with a razor blade (hereafter denoted as Ni–Ni(OH)$_2$). The following solution processed

activation is also rapid and simple, resulting in the in situ construction of a 3D sulfur-doped NiFe hydroxide shell to construct the core-shell membrane sample (denoted as Ni–S–NiFe(OH)$_2$) in 5 min at room temperature. The high flexibility of the membrane was well preserved (Figure S1D), indicating that the solution process resulted in limited surface modification. The thiosulfate ions promote corrosion reaction and formation of the S–NiFe(OH)$_2$ shell layer even at room temperature. A prolonged process time, such as ~1 h, led to the partial dissolution of the membrane, due to excessive corrosion of the Ni matrix by Fe^{3+} ions.[39] The nanostructure of the freestanding Ni–Ni(OH)$_2$ membrane was observed, as shown in Figure 2A,B. The intertwined 1D microfibers were found to be millimeter scale in length, with an average diameter of approximately 200 nm. Due to their high aspect ratio, exceeding a few thousands, these Ni–Ni(OH)$_2$ nanofibers, aligned by a uniform magnetic field line, could self-assemble into a freestanding flexible membrane. These nanofiber's high-aspect-ratio arrays were proven to have a strong capillary force, which easily absorbed water molecules onto the free-standing electrode.[25] As shown in Figure S2A,B, the maximum length of the aligned Ni–Ni(OH)$_2$ nanofibers could be extended to the centimeter scale by modifying the synthesis process (in our ongoing future project). In contrast to nickel foam, which exhibits pore sizes exceeding several 100 μm, the fibrous membrane
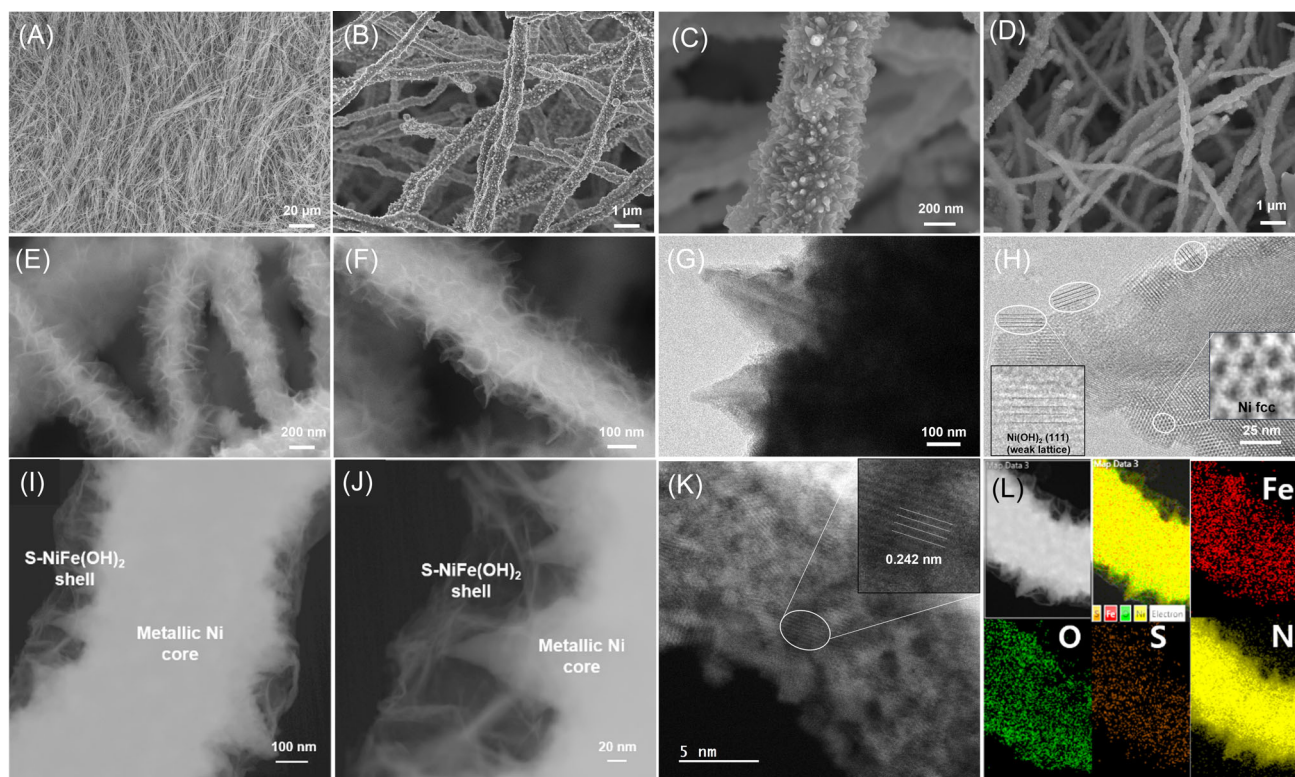
FIGURE 2 FE-SEM images of (A–C) Ni–Ni(OH)$_2$ and (D–F) Ni–S–NiFe(OH)$_2$ freestanding membrane. (G) HR-TEM and (H) HAADF-STEM images of Ni–Ni(OH)$_2$, and (I–K) Ni–S–NiFe(OH)$_2$. (L) STEM image and corresponding Ni, Fe, S, and O elemental mapping images, respectively.

catalysts feature pores on a markedly smaller scale, with dimensions less than 1 μm. This difference offers several advantages. For instance, their nanoscale pore structure offers an expanded surface area, increasing the number of active sites and significantly enhancing the efficiency of the catalytic reactions. Furthermore, the surface of the fibrous membrane catalyst allows for close contact between the various catalyst materials, thereby facilitating rapid charge transfer. In particular, as these structures consist of highly conductive interconnected metallic fibers, a uniform coating with catalysts such as metal oxides, which often suffer from low electrical conductivity, can greatly enhance charge transfer efficiency. This addresses the issue that can arise when a thick layer of metal oxide catalysts is deposited in the large pores of nickel foam, potentially obstructing charge transfer. In addition, it has been proven that the hierarchical 3D pore structure of the membrane catalyst promotes the release of gas bubbles.[19,25] This greatly helps to alleviate issues caused by vigorous gas evolution at high currents, which can impede access to the active sites of the electrolyte or cause the catalyst layer to peel off. After the room temperature activation process to generate the S–NiFe(OH)$_2$ overlayer, the overall fibrous structure was

found to be well preserved, as shown in Figure 2D. The detailed field emission scanning electron microscopy (FE-SEM) images in Figure 2E,F indicate the formation of core-shell structures. A thin ~20-nm-thick coating layer is formed on the surface of the nanofibers, with a nanosheet-like structure. The thickness of the S–NiFe(OH)$_2$ coating overlayer was controlled by the reaction time of the room temperature solution process. As shown in Figure S3A–C, the coating layer was ultrathin of less than ~10 nm for a reaction time of 1 min. As the reaction time was increased to 3 min (Figure S3D–F) and 20 min (Figure S3G–I), the diameters of the nanofibers increased up to the micrometer scale, and a nanosheet-coated matrix was generated between the fibrous network. Due to the contrast between the metallic Ni core and the S–NiFe(OH)$_2$ shell in the backscattered electron mode, they can be clearly distinguished, as shown in Figure S4A–C. The voids between the nanofibers were completely covered with the nanosheet-like matrix. The detailed nanostructure of the Ni–Ni(OH)$_2$ and Ni–S–NiFe(OH)$_2$ was observed by a high-resolution transmission electron microscope (HR-TEM). In Figure 2G of Ni–Ni(OH)$_2$, the horn-like surface of the nanofiber can be observed. The atomic-resolution high-angle annular dark field scanning transmission electron microscope

(HAADF-STEM) image in Figure 2H indicates that the core area of the horn is composed of ultra-small nanocrystals (Figure 2H). In the right inset image, a face-centered cubic nanostructure corresponding to metallic Ni is evident, and concurrently, a faint semi-crystalline structure, identifiable as the (002) plane of $Ni(OH)_2$ with a lattice fringe of approximately 0.24 nm, is discernible near the edge in the left inset image. After the coating process with S-doped $NiFe(OH)_2$, the nanofiber matrix was uniformly wrapped in the sheet-like shell layer (Figure 2I,J). The thickness of the outer shell was less than 10 nm (Figure S5). The HAADF-STEM image (Figure 2K) reveals the presence of numerous ultrasmall nanocrystals with a size of a few nanometers near the edges with lattice fringes of ~0.242 nm (inset image), indexed to the (012) facet of NiFe (oxy)hydroxide. In the STEM image presented in Figure 2L, along with the corresponding energy-dispersive X-ray spectroscopy (EDX) elemental mapping images, a uniform distribution of Fe, O, and S was observed across the entire nanofiber area, while the Ni signal exhibited some contrast at the core-shell interface. Line scanning EDX was performed for each element across the nanofiber, as shown in Figure S6A, and a diminished Ni signal at the core-shell interface was noted, as illustrated in Figure S6B. In the heterostructures of this nanofibrous matrix, the external shell consists of partially S-doped nickel (oxi)hydroxide, while the fibrous core network retains its reduced metallic nickel state. Previous reports in the literature suggest that milder solution-based synthesis conditions below 100°C typically induce the formation of a metal–hydroxide/sulfide interface[40] or sulfur doping in metal (oxy)hydroxide lattices.[41,42] For comparison, control samples designated $Ni(OH)_2$ and $S–NiFe(OH)_2$ were also prepared based on nickel foam. In this study, it is essential to distinguish the control samples from the membrane-type samples. The latter ones are capable of forming a wider array of heterostructures in their fibrous matrices and are denoted by an additional "Ni–" prefix in their labels. In contrast, this prefix is generally excluded from the labels of nickel-foam-based samples. A uniform coating of a sheet-like structure of either a $Ni(OH)_2$ layer (as shown in Figure S7A–C) or $S–NiFe(OH)_2$ (as depicted in Figure S7D–F) was observed on the nickel foam.

3.2 | Electronic structural analysis

In this study, the fibrous nickel network serves two key roles: it acts as a source of Ni ions to facilitate the growth of a highly oxidized, catalytically active shell layer and

ensures seamless charge transfer within membrane electrodes. Maintaining the integrity of the metallic fiber network is essential for efficient charge transfer. Forming an active shell layer that closely interfaces with the interconnected nickel network is also of paramount importance. Therefore, the formation of a heterostructure that localizes the highly oxidized shell domains on the nanofibrous surface was explored. To delve deeply into the localized formation of $Ni–S–NiFe(OH)_2$ heterostructures and area-specific chemical states, aberration-corrected STEM was employed using monochromated EELS. This technique can identify elements at atomic resolution and construct 2D image maps by analyzing the electronic structure or chemical bonding in specific areas.[43,44] First, a reference sample was selected, and powdery $Ni(OH)_2$ was obtained by detaching it from nickel foam using ultrasonication, which exhibited a nanosheet-like morphology (Figure S8A). Strong signals were observed in the electron energy loss near-edge structure (ELNES) spectra at the O K (Figure S8B) and Ni $L_{2,3}$ (Figure S8C) edges. The relative intensity ratio of the L_3 and L_2 edges of $Ni(OH)_2$ was calculated to be around 3.92, implying a relatively high oxidation state. Subsequently, EELS spectra near the surface edge of the $Ni–Ni(OH)_2$ nanofiber were visualized, as depicted in Figure 3A. Notably, the oxidation state at a single point, either at an interface or along the edges of the samples, was identified through EELS at the Ni $L_{2,3}$ and O K edges. The color contrasts observed in the same area indicate variations in the chemical states, distinguishing between metallic nickel in the bulk core area and oxidized nickel at the surface edge area. In comparison, overlaying the EELS Ni $L_{2,3}$ edge spectra from the bulk core (indicated as "core") and the surface edge (indicated as "shell") areas in Figure 3B verifies these different relative intensity ratios of L_3/L_2 edges. Similar trends representing the oxidized state near the surface edge of the Ni nanofiber could also be observed in the line-scanning EELS profile (Figure S9A–C). In other words, as the EELS spectrum is obtained while scanning from the bulk to the surface edge direction, a gradually stronger signal is observed at the O K edge (Figure S9B), and conversely, the relative signal of the Ni L_2 edge weakens compared to the Ni L_3 edge signal (Figure S9C). A heterostructure consisting of a metallic Ni core and a highly oxidized $Ni(OH)_2$ shell has previously demonstrated exceptional HER activity in alkaline conditions.[25,45,46] In this heterostructure, electrons move rapidly along the fibrous nanofibers, while the highly oxidized metal hydroxides shell adsorb OH^- ions and catalyze electrochemical reactions. The formation of the $Ni–Ni(OH)_2$ heterostructure near the surface edge was further investigated (Figure S10A). Selected area electron diffraction (SAED)
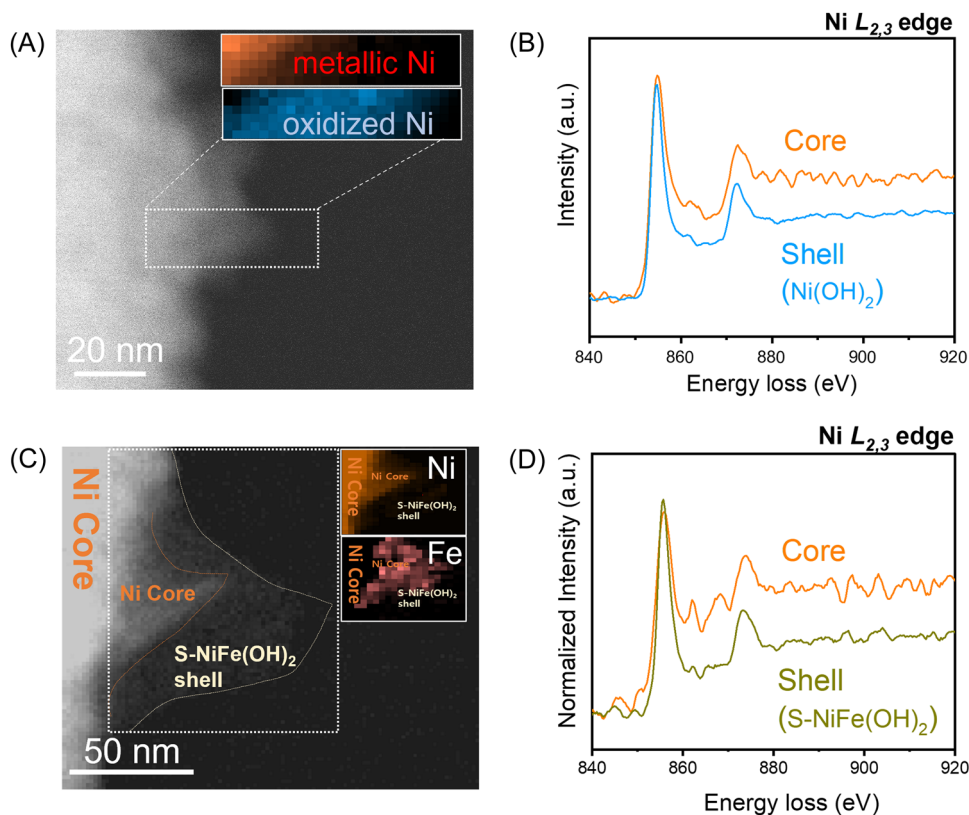
FIGURE 3 (A) ADF-STEM image of Ni–Ni(OH)$_2$ and the area (dotted box) selected for EELS acquisition, with inset images depicting constructed 2D illustrations of Ni (top inset) and oxidized Ni (bottom inset) spectra. (B) Comparison of EELS Ni $L_{2,3}$ edge for the core and shell area. (C) ADF-STEM image of Ni–S–NiFe(OH)$_2$ and the designated area (dotted box) for EELS acquisition. Inset images represent constructed 2D illustrations for Ni (top inset) and Fe (bottom inset). (D) Comparison of EELS Ni $L_{2,3}$ edge for core and shell area of Ni–S–NiFe(OH)$_2$.

patterns were obtained separately from the bulk area (Figure S10B) and the surface edge area (Figure S10C). The typical d-spacings, calculated from the bulk and surface edge areas, were found to be ~0.204 and ~0.243 nm, respectively, corresponding to the (101) plane of metallic Ni and the (002) plane of Ni(OH)$_2$. Postair exposure, which led to the further formation of the surface (oxy)hydroxide layer, an EELS line scan was again conducted across the Ni–Ni(OH)$_2$ interface (Figure S11A). This resulted in observations of normalized relative intensities between Ni and O that displayed a marked difference at the boundary, as depicted in Figure S11B. Tracing the line profile from the core to the surface area, the relative intensity of oxygen is zero at the starting point of the bulk area, but it shows a sharp increase near the surface edge, signifying an oxidized surface. The HR-TEM image in Figure S11C further reveals distinct areas between metallic Ni and Ni(OH)$_2$ with varying d-spacings of 0.204 and 0.243 nm, respectively. Similarly, an image from EELS using the Ni $L_{2,3}$, O K, and

Fe L edges was constructed for the powder S–NiFe(OH)$_2$ sample with a nanosheet-like morphology (Figure S12A,B), which was detached from nickel foam. Distinct signals appear in the EELS spectra for Ni (Figure S12C) and Fe (Figure S12D). Additionally, the Ni and Fe signals (Figure S12E,F) are evenly distributed across the entire area. In contrast, in the EELS mapping image collected near the edge surface area of the Ni–S–NiFe(OH)$_2$ (Figure 3C), a sharp color contrast is apparent between the Ni core and S–NiFe(OH)$_2$ shell areas, as shown in the inset images. The ELNES spectra of the Ni $L_{2,3}$ edge for each specific area were compared, as shown in Figure 3D, and the relative intensity ratio of L_3/L_2 of the shell area was found to be much higher than that in the core area, demonstrating the difference in oxidation states and the formation of a heterostructure boundary. In the TEM image focusing on the near-surface edge area of Ni–S–NiFe(OH)$_2$ (Figure S13A), HR-TEM images and corresponding SAED patterns were collected for three distinct areas, as indicated in the image. The d-spacings observed in the areas
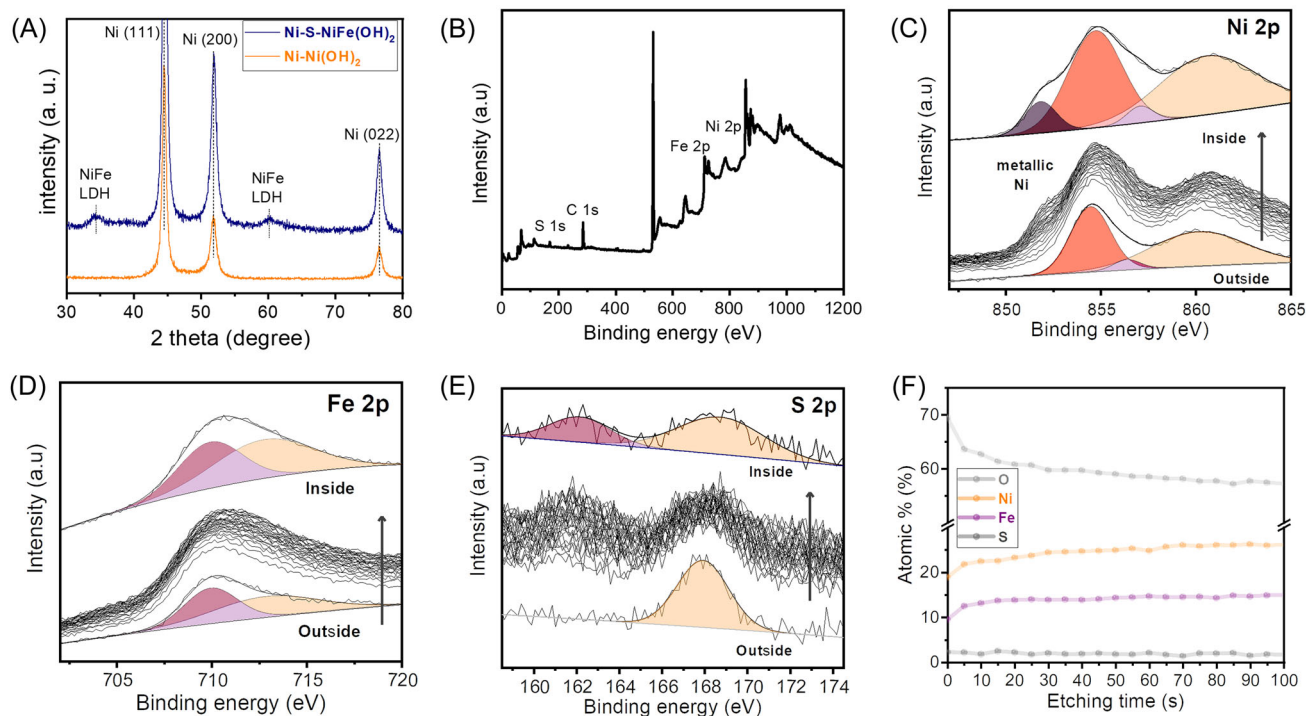
FIGURE 4 (A) XRD patterns of the samples. (B) XPS survey spectrum and corresponding depth profiles of (C) Ni 2p, (D) Fe 2p, and (E) S 2p spectra of Ni–S–NiFe(OH)$_2$. (F) The atomic ratio of each element with etching time.

displayed in Figure S13B,C were 1.75 and 1.99 Å, respectively, and were indexed to the (200) and (111) planes of metallic Ni. Conversely, the observed d-spacing of approximately 2.41 Å, as shown in Figure S13D, can be attributed to NiFe (oxy)hydroxide. The crystalline structures of Ni–Ni(OH)$_2$ and Ni–S–NiFe (OH)$_2$ were analyzed by thin-film X-ray diffraction (XRD) diffraction patterns, as shown in Figure 4A. The three main peaks observed for Ni–Ni(OH)$_2$ were indexed to the (111), (200), and (220) facets of metallic Ni (JCPDS No. 04-0850). Furthermore, two broad peaks emerged in Ni–S–NiFe (OH)$_2$, located at 34° and 61°, which can be assigned to NiFe layered double hydroxide (JCPDS No. 49-0188). Similar XRD patterns were observed for the control group, Ni(OH)$_2$ and S–NiFe(OH)$_2$ grown on nickel foam (Figure S14A,B), including metallic Ni peaks, due to the presence of the nickel foam substrate. X-ray photoelectron spectroscopy (XPS) was conducted on the Ni–S–NiFe(OH)$_2$ membrane to investigate its chemical composition and oxidation state. The survey spectrum confirmed the presence of Ni, Fe, S, and O elements (Figure 4B), with S constituting about 2.2% of the atomic ratio. To further elucidate the formation of the heterostructure of the metallic core and the oxidized surface shell, argon ion beam etching was implemented. The XPS scan was repeated after each 5-s etching interval for 40 cycles. The fine Ni 2p spectrum (Figure 4C) initially revealed a broad

Ni 2p$_{3/2}$ peak at ~854.5 eV, attributed to the oxidized Ni state. A zero-valence Ni peak emerged gradually at 851.0 eV as the etching process proceeded, indicative of the metallic nickel core. The fine Fe 2p spectrum displayed two broad peaks from the Fe^{3+} oxidation state, which remained largely unchanged after etching (Figure 4D). In the S 2p spectrum (Figure 4E), the primary peak at ~168.5 eV was initially noticed, correlating to partially oxidized S elements on the catalyst surface.[41] A broad peak at ~161.7 eV emerged during etching, suggesting that sulfur atoms substituted for O in the NiFe(OH)$_2$ lattice, rather than forming metal sulfides. The O 1s fine XPS spectrum (Figure S15) displayed a reduction in peaks at ~529.3 and ~531.5 eV after the etching process, associated with metal–oxygen and metal–hydroxide groups, respectively. Figure 4F shows that the initial etching effectively reduced the atomic oxygen ratio, signifying an oxidized ultrathin overlayer. The oxygen ratio further diminished with an increase in etching duration, simultaneously escalating the ratio of the Ni and Fe elements. For comparative purposes, the fine Ni 2p spectra of Ni(OH)$_2$ (Figure S16A), S–NiFe (OH)$_2$ (Figure S16B), and Ni–Ni(OH)$_2$ (Figure S16C) are also presented. As shown in Figure S17, the main Ni 2p$_{3/2}$ peak of Ni–Ni(OH)$_2$ and Ni–S–NiFe(OH)$_2$ was at ~855.3 eV, showing a negative shift of approximately 1.0 eV compared to ~856.3 eV of Ni(OH)$_2$ and S–NiFe (OH)$_2$. This indicates a partially reduced and

oxygen-deficient state, attributable to the mixed phases of Ni, Ni(OH)$_2$, and/or S–NiFe(OH)$_2$. A similar negative shift in the Ni 2p spectra was also previously observed and reported in electrodeposited Ni–Ni(OH)$_2$,[47] and this shift can be explained by the formation of weaker Ni–OH bonds within β–Ni(OH)$_2$. This can lead to stronger hydrogen bonding interactions with water molecules in alkaline media. Additional XPS spectra including the survey spectrum (Figure S18A), fine Fe 2p (Figure S18B), and S 2p (Figure S18C) of S–NiFe(OH)$_2$ were also obtained and showed results similar to those of Ni–S–NiFe(OH)$_2$. To investigate the role of sulfur doping in the following electrochemical performance, additional sulfur-free control samples were prepared using nickel foam or Ni–Ni(OH)$_2$ membrane by immersing them in a solution of Fe (NO$_3$)$_3$·9H$_2$O under ambient conditions following the literature.[48] The formation of a uniform sheet-like morphology of NiFe(OH)$_2$ nanosheets deposited on the nickel foam was confirmed (Figure S19A–C), as well as on Ni–Ni(OH)$_2$ (Figure S20A,B), denoted as NiFe(OH)$_2$ and Ni–NiFe(OH)$_2$, respectively. In the Raman spectroscopy results (Figure S21), S–NiFe(OH)$_2$ showed a strong and sharp peak at around 457 cm^{-1}, representing the Ni–OH bond. In contrast, Ni–S–NiFe(OH)$_2$ exhibited broad peaks at approximately 463 and 558 cm^{-1}, stemming from the Ni–OH stretching mode of Ni(OH)$_2$ and the Ni–O vibrational mode of NiOOH, respectively.[47,49,50] The Fe–O vibrational mode of FeOOH was also observed at around 677 cm^{-1}, indicating the formation of Ni and Fe hydroxides on the surface of Ni–S–NiFe(OH)$_2$. This composition has previously been reported in the literature for nickel (oxy)hydroxide samples synthesized by a solution process under a reducing atmosphere.[25,47] During the water electrolysis reaction, Ni and Fe interact and are structurally reconstructed, which can further improve the catalytic activity of the NiFe (oxy)hydroxide catalyst by generating NiOOH and FeOOH phases.[51] For instance, high-valence Ni such as that in γ-NiOOH contributes to OER activity, and the presence of Fe assists in water dissociation in HER.[52]

3.3 | Electrochemical analysis

The electrochemical properties of the as-prepared samples were investigated in 1 M KOH electrolytes using a typical three-electrode configuration. As shown in Figure 5A, LSV curves confirm the extraordinary HER catalytic activities of the freestanding membrane-type catalyst electrodes, greatly surpassing those of nickel-foam-based electrodes and Pt/C catalysts. Among them, Ni–S–NiFe(OH)$_2$ exhibited the highest catalytic activity with overpotential values of $\eta_{10} = 25.2$, $\eta_{100} = 61.1$, and

$\eta_{1000} = 198.0$ mV at current densities of 10, 100, and 1000 mA cm^{-2}, respectively, much smaller compared to those of S–NiFe(OH)$_2$ ($\eta_{10} = 167$, $\eta_{100} = 300$ mV) and even Pt/C catalysts ($\eta_{10} = 27.5$, $\eta_{100} = 89.9$ mV). Notably, the freestanding membrane-type electrodes exhibited exceptional HER activity not only at high current densities but also at current densities less than 100 mA cm^{-2}. As shown in Table S1, the HER activity of Ni–S–NiFe(OH)$_2$ ranks among the top levels when compared to the state-of-the-art HER catalysts, including NiMo-based catalysts.[17,18,20,23,25,36,47,53–55] The electrode we present is both highly active and cost-effective unlike the NiMo-based or metal chalcogenide catalyst electrodes that require complex, time-intensive, and expensive preparation procedures. For instance, metal chalcogenide electrodes necessitate a two-step process that includes hydrothermal reactions at temperatures above 100°C in stainless steel autoclaves, followed by sulfidation or phosphidation at temperatures exceeding 350°C under an argon atmosphere. We have detailed the synthesis methods and specific conditions in Tables S1–S3 for further comparison. As shown in Figure 5B, the Tafel slope of Ni–S–NiFe(OH)$_2$ was extremely small at 14.1 mV dec^{-1}, which is much smaller than that of S–NiFe(OH)$_2$ (80.6 mV dec^{-1}), indicating the more favorable HER kinetics and efficient charge transfer of the membrane-type electrodes. EIS was used to examine the series resistances of the samples. As depicted in the Nyquist curves in Figure S22A, R_{HFR} and the charge transfer resistance (R_{ct}) of the membrane-type samples were considerably lower than those of the nickel-foam-based samples. The observed low R_{HFR} in the membrane-type samples compared to the nickel-foam-based samples can be attributed to the combination of subresistances of the electrode resistance ($R_{electrode}$) and $R_{solution}$. Given that the distance between the electrodes is similar, resulting in comparable $R_{solution}$ values, the reduced R_{HFR} can be attributed to minimized $R_{electrode}$. This advantage stems from the electrically conductive interconnected metallic fibrous matrices and the substrate-free nature of the freestanding membrane-type electrodes. In a related trend, the R_{HFR} of the S–NiFe(OH)$_2$ sample, prepared by direct growth of the catalyst on 3D nickel foam, was lower than that for the Pt/C sample, which was prepared by depositing a dense catalyst layer onto a planar carbon-nanofiber-paper substrate. It is worth noting that the iR correction in this study relied on an on-the-fly correction of positive feedback. A proper initial R_{HFR} value for each sample, as outlined in recent literature,[13] was chosen to ensure the reliability of the catalyst activity readings, especially at high current densities. In addition, the multistep chronopotentiometric curves for Ni–Ni(OH)$_2$, Ni–NiFe(OH)$_2$, and Ni–S–NiFe(OH)$_2$ were recorded at
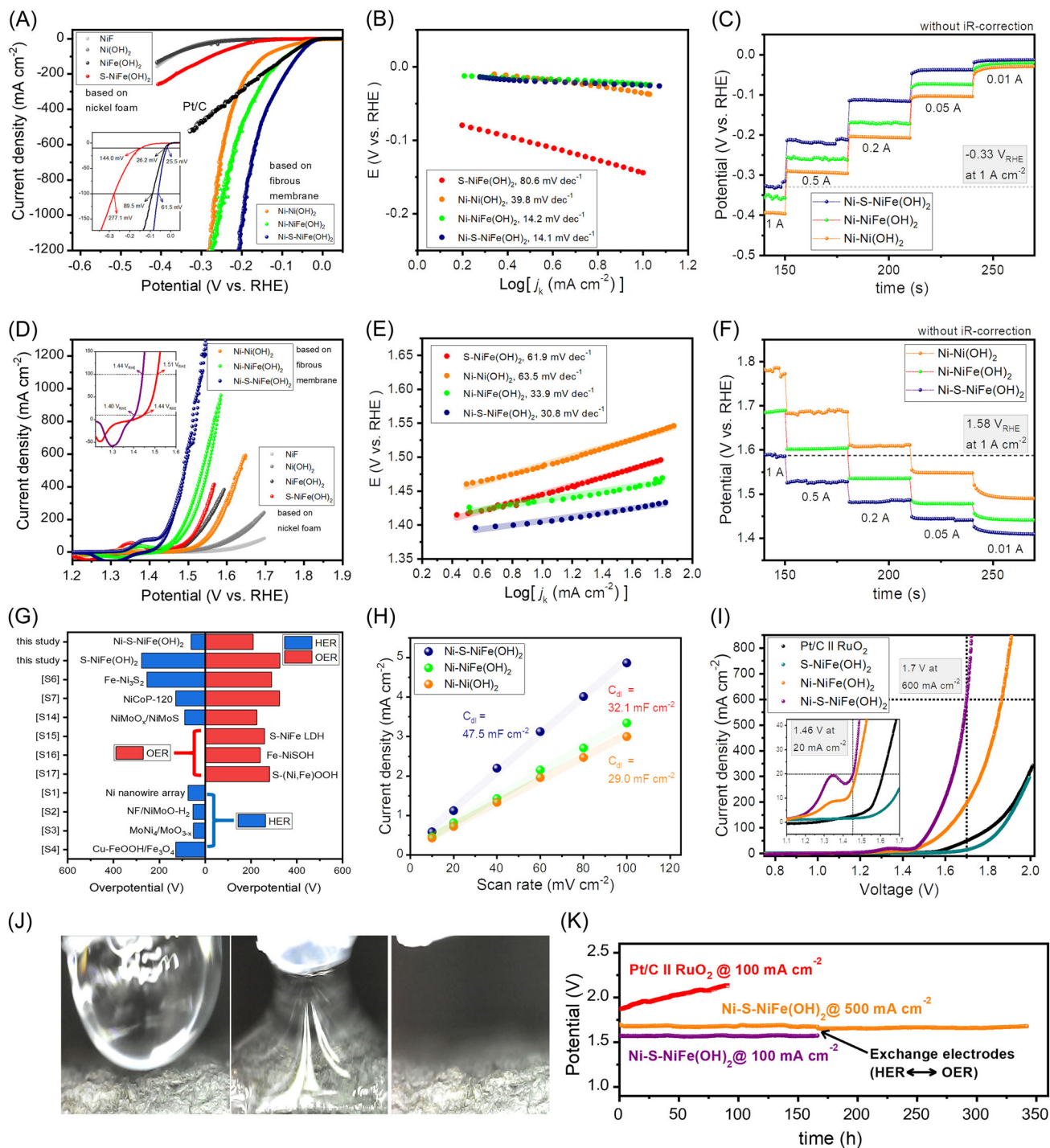
FIGURE 5 (A) LSV curves comparing nickel foam-based, freestanding membrane-based, and Pt/C samples in 1 M KOH electrolyte at a scan rate of $0.2\,\mathrm{mV\,s^{-1}}$; inset image illustrating the contrast of Ni–S–NiFe(OH)$_2$, S–NiFe(OH)$_2$, and Pt/C samples. (B) Corresponding Tafel plots. (C) Multistep chronopotentiometric profiles at various densities without iR correction. (D) CV curves and reverse-direction LSV curves in 1 M KOH electrolyte at a scan rate of $1\,\mathrm{mV\,s^{-1}}$; the inset image recording the backward direction. (E) Corresponding Tafel plots. (F) Multistep chronopotentiometric curves without iR correction. (G) Comparative evaluation of the overpotential required at a current density of $100\,\mathrm{mA\,cm^{-2}}$ for HER and OER with recently reported state-of-the-art electrocatalysts, as detailed in Tables S1 and S2. (H) Capacitive current density against various scan rates. (I) LSV curves for a two-electrode system using bifunctional S–NiFe(OH)$_2$, Ni–NiFe(OH)$_2$, and Ni–S–NiFe(OH)$_2$ electrodes, alongside precious metal electrodes by coupling Pt/C and RuO$_2$ electrodes in 1 M KOH electrolyte at a scan rate of $1\,\mathrm{mV\,s^{-1}}$. (J) Digital images assessing the adsorption properties of Ni–S–NiFe(OH)$_2$, capturing the instance of water droplet dropping. (K) Chronoamperometric curves of Ni–S–NiFe(OH)$_2$‖Ni–S–NiFe(OH)$_2$ and Pt/C‖RuO$_2$ water electrolyzers at current densities of 100 and/or $500\,\mathrm{mA\,cm^{-2}}$ in 1 M KOH electrolyte.

various current densities. These measurements were conducted without iR correction to evaluate the activity, as shown in Figure 5C. As the applied current densities were increased up to $1.0\,A\,cm^{-2}$, the recorded overpotential of Ni–S–NiFe(OH)$_2$ toward HER remained less than ~330 mV. Compared to those of S–NiFe(OH)$_2$, it required an overpotential value of 1300 mV to produce $1.0\,A\,cm^{-2}$ of current density in HER (Figure S23A), indicating a significant loss of electricity to produce the same amount of hydrogen. Additionally, it is worth noting that the formation of the Ni–Ni(OH)$_2$ heterostructure was crucial to catalytic activity, particularly for HER. Intriguingly, the Ni–Ni(OH)$_2$ membrane sample without the drying process (with only a washing process) showed much inferior HER activity (not shown) due to the prohibited contact with air atmosphere and the natural formation of a Ni(OH)$_2$ layer. Subsequently, the OER electrocatalytic activities in 1.0 M KOH electrolyte were investigated by CV at a slow scan rate of $1\,mV\,s^{-1}$ to avoid overestimation, which might arise from the overlapping of the redox reactions of the nickel species, and the overpotential values were acquired from the backward CV scan. Figure 5D reveals that Ni–S–NiFe(OH)$_2$ exhibited the lowest overpotential values of $\eta_{10} = 174$, $\eta_{100} = 204$, and $\eta_{1000} = \sim 270$ mV at 10, 100, and $1000\,mA\,cm^{-2}$, respectively, compared to other samples including S–NiFe(OH)$_2$ ($\eta_{10} = 230$ mV and $\eta_{100} = 280$ mV). This OER activity was superior to that of the recently reported best-performing OER catalysts.[33,39,41,49,56,57] The OER catalytic activity of Ni–Ni(OH)$_2$ was boosted with the addition of Fe and S species, a trend that was also observed in the nickel foam-based samples. In the Tafel plots in Figure 5F, a much smaller Tafel slope for Ni–S–NiFe(OH)$_2$ of $30.8\,mV\,dec^{-1}$ was observed, compared to that of Ni–Ni(OH)$_2$ ($63.5\,mV$ dec^{-1}), Ni–NiFe(OH)$_2$ ($33.9\,mV\,dec^{-1}$), and S–NiFe(OH)$_2$ ($61.9\,mV\,dec^{-1}$), demonstrating its rapid OER kinetics. The superior OER activity of Ni–S–NiFe(OH)$_2$ can also be confirmed by both the smaller R_{HFR} and R_{ct} values in Figure S22B. The multistep chronopotentiometric measurements shown in Figure 5F substantiate that the applied potential was ~1.59 V_{RHE} at a current density of $1\,A\,cm^{-2}$ without iR correction. This is notably lower than the ~2.4 V_{RHE} recorded for S–NiFe(OH)$_2$ needed to produce an identical current density (Figure S23B). A comparative evaluation of the overpotentials required at a current density of $100\,mA\,cm^{-2}$ for both HER and OER, with the recently reported state-of-the-art electrocatalysts, is presented in Figure 5G. To estimate the electrochemical surface area (ECSA) of the freestanding membrane samples, the C_{dl} values were calculated from the CV curves at various scan rates (Figure S24A–C). As shown in Figure 5H, the C_{dl} value of Ni–S–NiFe(OH)$_2$ was

$47.5\,mF\,cm^{-2}$, which is higher than that of Ni–Ni(OH)$_2$ ($29.0\,mF\,cm^{-2}$) and Ni–NiFe(OH)$_2$ ($32.1\,mF\,cm^{-2}$) indicating the larger ECSA. For comparative analysis, fully sulfurized control samples were produced using a thermal sulfurization method at 350°C. This involved transforming Ni–Ni(OH)$_2$ and Ni–S–NiFe(OH)$_2$, as shown in Figure S25A–D, respectively. The resultant samples were accordingly designated as Ni–NiS and Ni–NiFeS. The XRD patterns in Figure S26A,B confirm the successful formation of the NiS (JCPDS card No. 02-1280) and NiS$_2$ (JCPDS card No. 11-0099) crystalline phases in both the Ni–NiS and Ni–NiFeS samples. The bifunctional activities of the two samples were evaluated as shown in Figure S27A,B. The fully sulfurized metal sulfide samples exhibited much lower bifunctional activity compared to Ni–S–NiFe(OH)$_2$ and also lost good flexibility after the thermal sulfurization process. These results imply that optimizing bifunctional activity depends on the formation of abundant heterostructures. In previous studies, these hetero-structured catalytic electrodes provided much more optimized catalytic performance compared to single-phase metal oxyhydroxides or metal sulfide, due to the synergistic effects generated between the metallic support and the metal derivative nanodomains acting as active sites.[40,58] The significant difference in HER activity between S–NiFe(OH)$_2$ and Ni–S–NiFe(OH)$_2$ can be explained by the presence of the highly conductive Ni-nanofiber matrix. First, these nanofiber matrices can provide a much larger ECSA and numerous exposed active sites compared to nickel foam with its macroporous structure. In addition, for S–NiFe(OH)$_2$ grown on a nickel foam substrate, the charge transfer may be hindered due to the low electrical conductivity of the metal oxyhydroxide, resulting in a series resistance within the catalyst layer and at the interface with the nickel foam. On the other hand, the fully interconnected fibrous nickel network featuring Ni–S–NiFe(OH)$_2$ can provide excellent electronic conductivity, promoting efficient charge transfer within the heterostructures formed on the nanofiber surface. Lastly, these fibrous structures in the freestanding membrane-type electrode exhibit high voltage for practical electrochemical cells for industrial-scale hydrogen production, which is primarily hindered by charge and mass transport limitations at high current densities. Another associated consideration is the strong gas bubbling observed at high currents, which can interfere with the liquid electrolyte access to the active sites or cause the delamination of the catalyst layer. Inspired by the excellent bifunctional catalytic activities, the electrochemical performances of OWS with membrane-type samples were investigated in 1.0 M KOH electrolyte. As shown in Figure 5I, the alkaline

water electrolyzer with two pieces of Ni–S–NiFe(OH)$_2$ electrodes exhibited voltage values of only 1.46, 1.53, and 1.70 V to produce current densities of 20, 100, and 600 mA cm^{-2}, respectively. The impressive superior performance of this system compared to other OWS systems (Table S3) at all current densities allows the efficient optimization of hydrogen production under a wide range of operating conditions, from around 10 mA cm^{-2} for single solar panel applications to ampere-scale current densities targeting high-demand business scenarios. In comparison, the other systems required much higher voltage values at the same current densities, that is, 100 mA cm^{-2} (1.61 V for Ni–NiFe(OH)$_2$∥Ni–NiFe(OH)$_2$, 1.82 V for Pt/C(−)∥RuO$_2$(+), and 1.86 V for S–NiFe(OH)$_2$∥ S–NiFe(OH)$_2$). The oxygen and hydrogen gases generated during the chronoamperometric test at a current density of 100 mA cm^{-2} were separately collected, as shown in Figure S28. The relative evolved amount of hydrogen and oxygen gas was 2:1, and ~100% of Faradaic efficiency was recorded, as shown in Figure S29. The super-hydrophilic nature as well as the nanofibrous matrix leads to the excellent bubble releasing ability of the catalytic electrode,[19,59–61] which is another important consideration for OWS at high current densities. Next, the absorption of water droplets into the S–NiFe(OH)$_2$ and Ni–S–NiFe(OH)$_2$ was recorded using a digital microscope (Videos S1 and S2, respectively). As shown in Figure 5J, the rapid uptake of water droplets onto Ni–S–NiFe(OH)$_2$ occurred over the entire surface and completely penetrated the freestanding membrane. Similarly, the hydrophilic nature of S–NiFe(OH)$_2$ and the absorption of water droplets into the porous structure of the nickel foam were observed, as shown in Figure S30. The bubble release behavior of S–NiFe(OH)$_2$ (Video S3) and Ni–S–NiFe(OH)$_2$ (Video S4) was recorded at an applied current density of 100 mA cm^{-2}. The formation and growth of relatively large gas bubbles of ~100 μm were observed in S–NiFe(OH)$_2$, and bubbles were observed to be trapped in the macropores of the nickel foam (Figure S31A). In comparison, the pore size of Ni–S–NiFe(OH)$_2$ was much smaller, and the evolved gas molecules were released quickly before large bubbles appeared, as shown in Figure S31B. The stability of alkaline water electrolyzers assembled from two Ni–S–NiFe(OH)$_2$ membranes or two asymmetric electrodes of Pt/C and RuO$_2$ was evaluated by chronoamperometric measurements at current densities of 100 and/or 500 mA cm^{-2}. As shown in Figure 5K, the applied voltage for the Ni–S–NiFe(OH)$_2$∥Ni–S–NiFe(OH)$_2$ system was recorded at 1.57 and 1.66 V at current densities of 100 and 500 mA cm^{-2}, respectively, and was well maintained without obvious change in the 1 M KOH

electrolyte for ~150 h of operation time. Interestingly, the two electrodes in the OWS system can be substituted for each other, and the voltage of ~1.66 V in the OWS system with exchanged HER and OER electrodes was maintained for another ~150 h without significant voltage change. In contrast, the alkaline water electrolyzer with Pt/C∥RuO$_2$ electrodes showed poor stability with gradually increased applied voltage by OWS at 100 mA cm^{-2}.

3.4 | First-principles DFT calculations

To track the origin of the bifunctional electrocatalytic activities and simulate the energetics of various HER/OER intermediates, first-principles calculations were performed. Slab models of Ni(OH)$_2$, NiFe(OH)$_2$, and S-doped NiFe(OH)$_2$ were constructed as shown in Figure 6A. The (110) crystal plane was selected as the active surface according to the previous literature.[62] Upon the introduction of S species, the doping mechanism follows the sequence of OH defect formation and S-doping on the defect site (Figure 6B). The most favorable doping site can be estimated to be O1, the oxygen on the outermost surface of the NiFe (OH)$_2$, as both its oxygen defect formation energy and doping energy were the least among the possible doping sites. The total doping energy was O1 (0.91 eV) < O2 (1.33 eV) < O3 (2.81 eV). The theoretical OER activity was predicted using a Gibbs free energy diagram with the widely accepted four-electron adsorbate oxygen evolution mechanism as shown in Figure 6C (see Section S2.8— Computational methods for details). The rate-determining step was transformed from the process (OH* → O*) with Gibbs free energy of ΔG_2 for Ni(OH)$_2$ and NiFe(OH)$_2$ to the process (OOH* → O$_2$) with Gibbs free energy of ΔG_2 for S–NiFe(OH)$_2$. The doping strengthened the adsorption on Ni, the active site, which was also predicted by the more negative integrated crystal orbital hamilton population value, as shown in Figure 6E. The stronger adsorption on the catalyst makes it difficult to desorb O$_2$; however, the increased adsorption energy decreases the change in free energy leading to the reduction in overpotential. The trend of OER activity can be stated as Ni(OH)$_2$ (1.19 V) > NiFe(OH)$_2$ (0.75 V) > S–NiFe(OH)$_2$ (0.30 V). Doping also enhanced the HER activity, as shown in Figure 6D,E. The activity of HER was analyzed from both thermodynamic and kinetic perspectives. The Gibbs free energy of each electrocatalyst followed the order of S–NiFe(OH)$_2$ (0.92 eV) < NiFe(OH)$_2$ (1.02 eV) < Ni(OH)$_2$ (1.94 eV), suggesting that the barrier was lessened for S–NiFe(OH)$_2$. It is well known that the activation barrier between H$_2$O and H*–OH* state is crucial in alkaline media. In Figure 6E,
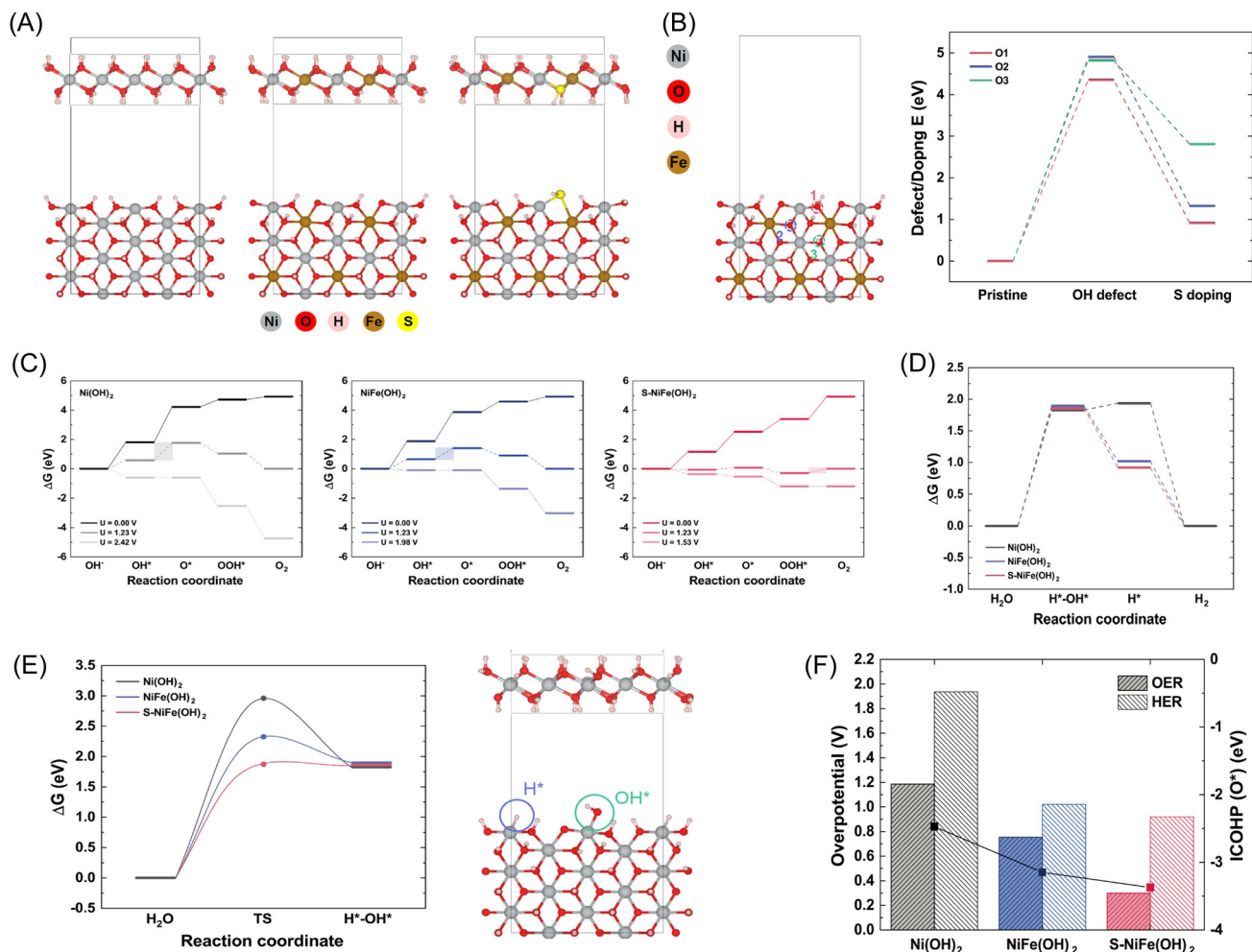
FIGURE 6 First-principles calculations to simulate the bifunctional activity. (A) The constructed structure models, (B) the calculation for favorable S doping sites, (C) the reaction energy diagram toward different reaction intermediates at different stages of OER, (D) the reaction energy diagram toward HER, (E) the predicted H_2O dissociation barrier, and (F) the summary of the simulated OER and HER trends.

S-doping drastically reduced the activation barrier, implying enhanced HER activity. The activation barrier was decreased in the order of S–NiFe(OH)$_2$ (1.87 eV), NiFe(OH)$_2$ (2.32 eV), and Ni(OH)$_2$ (2.96 eV). Finally, the catalytic activity trends of three different lattice models for both OER and HER are summarized in Figure 6F, and it can be concluded that the required overvoltage for OWS of S–NiFe(OH)$_2$ in alkaline media was much smaller than that of Ni(OH)$_2$ and NiFe(OH)$_2$.

3.5 | The operational stability and performance of a symmetric AEM water electrolyzer

The reversibility of the bifunctional catalyst provides an additional advantage for the practical operation of an AEM water electrolyzer. Operating stability issues[34,36,63,64]

induced by dynamic operating conditions have recently emerged in practical water electrolysis systems. The primary stability issues of catalyst electrodes stem from changes in dynamic structure under anodic and/or cathodic polarization or poor reversibility of chemical states. For instance, the activity of a NiFe hydroxide anode in the OER oxidation state suffered from degradation above the relatively high current density of 100 mA cm^{-2},[29] mainly due to the irreversible structural change related to its poor structural stability. Similarly, reverse current generation during the shut-down period led to the irreversible oxidization of metallic Ni or Fe cathodes to metal (oxy)hydroxide phases, leading to a degradation in performance during alkaline water electrolysis[14] and requiring an additional cathodic protection strategy.[34] As illustrated in Figure 7A, the operating stability and reversibility of the bifunctional Ni–S–NiFe(OH)$_2$ for both OER and
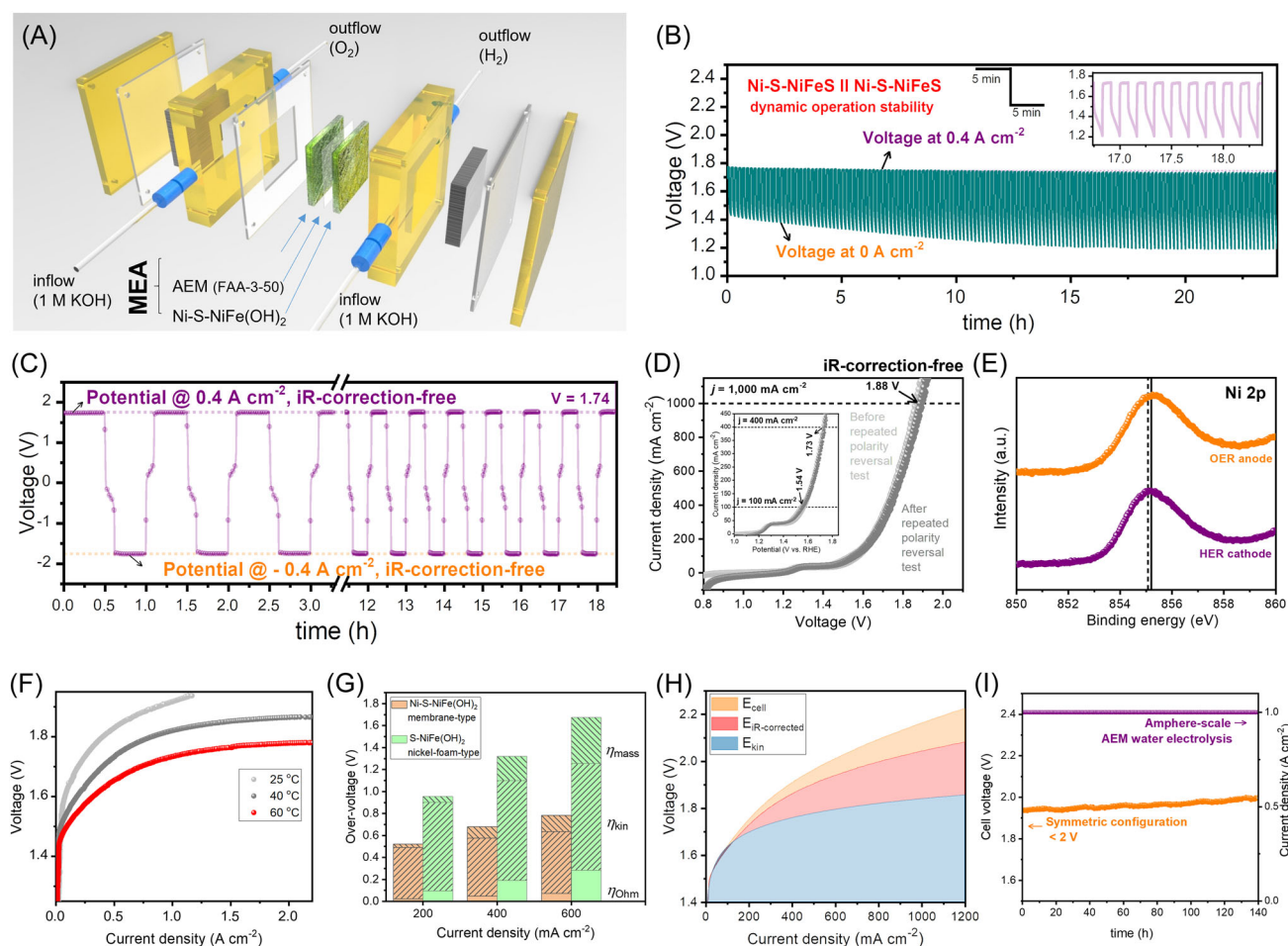
FIGURE 7 (A) Schematic representation of a symmetric AEM water electrolysis system. (B) Chronopotentiometric curve for Ni–S–NiFe (OH)$_2$‖Ni–S–NiFe(OH)$_2$, illustrating the on–off test results at 0.4 and 0 A cm^{-2} with 5-min intervals. (C) Chronopotentiometric curve for a symmetric water electrolysis system employing two Ni–S–NiFe(OH)$_2$ electrodes, where a current density of 0.4 A cm^{-2} is applied with polarity reversal every 30 min for 18 h. (D) LSV curves representing the overall water splitting activity of Ni–S–NiFe(OH)$_2$ before and after the repeated polarity reversal test. (E) Comparative analysis of high-resolution XPS in Ni 2p spectra for Ni–S–NiFe(OH)$_2$ anode and cathode postdurability tests. (F) Polarization curves of Ni–S–NiFe(OH)$_2$‖Ni–S–NiFe(OH)$_2$ at different temperatures. (G) Analysis of the overvoltages in two alkaline electrolyzers operating at room temperature, detailing the η_{ohm}, η_{kin}, and η_{mass} across various current densities. (H) The cell voltage, iR-corrected cell voltage, and kinetic voltage. (I) Chronopotentiometry curve at room temperature of Ni–S–NiFe(OH)$_2$‖Ni–S–NiFe (OH)$_2$ system during ampere-scale AEM water electrolysis.

HER were analyzed in a symmetric AEM water electrolysis system using a 1 M KOH electrolyte at 25°C. It should be noted that the practical performance of the AEM electrolyzer was assessed without iR correction. Figure 7B, featuring chronopotentiometry curves, emphasizes the remarkable dynamic stability of the system with the Ni–S–NiFe(OH)$_2$‖Ni–S–NiFe(OH)$_2$ electrodes. This stability was confirmed during transient on–off cycles over a 24-h period, with current densities alternating between 0.4 and 0 A cm^{-2} for intervals of 5 min each. The applied voltage at 0.4 A cm^{-2} was ~1.74 V, and it was well preserved during on–off cycles, indicating superb operational stability. Furthermore, the reversibility of this system was also evaluated by the

repeated polarity reversal test, as shown in Figure 7C. Initially, a constant current density of 0.4 A cm^{-2} was applied to this system and maintained for 30 min, during which the applied voltage was observed to be 1.74 V. Afterward, the polarity of the system was switched every 30 min, and for 36 reversals (i.e., 18 h), the voltage did not show any noticeable changes, demonstrating outstanding durability and preserving performance under dynamic operating conditions. This indicates that each HER and OER reversible bifunctional electrode can be replaced during operation; that is, a used OER electrode can replace a failed HER electrode or vice versa. This is feasible regardless of the operating conditions, whether under oxidation or

reduction states. As shown in Figure 7D, the water electrolysis performances of this symmetric system were recorded at 1.54, 1.73, and 1.88 V to produce current densities of 100, 400, and 1000 mA cm^{-2}, respectively, without iR correction. This performance was retained after the repeated polarity reverse test, without a noticeable change in LSV curves. To track the excellent reversibility and stability of the Ni–S–NiFe(OH)$_2$ electrode, the structural and chemical changes of each electrode after the stability test in the above water electrolysis system were investigated by conducting SEM, XRD, XPS, and Raman analyses. The original 1D nanofiber structure was well preserved after stability tests in HER (Figure S32A–C) or OER (Figure S33A–C) side electrodes, and the nanosheet-like morphology was clearly retained in both electrodes. In the XRD pattern in Figure S34, the metallic Ni peaks were well preserved in the HER-side electrode, while the peaks observed in the OER-side became slightly broader due to surface oxidation. In addition, a new shoulder peak observed at 44.2° can be assigned to metallic NiFe, indicating the possible structural interaction of Ni and Fe during OER. HR-TEM images (Figure S35A–D) showed the well-preserved overall nanostructure of Ni–S–NiFe(OH)$_2$ after the stability test, without any significant change. Fine Ni 2p (Figure S36A,B) and Fe 2p (Figure S36C,D) spectra of Ni–S–NiFe(OH)$_2$ after the stability test also showed no significant changes. In the comparison of the XPS Ni 2p (Figure 7E) and Fe 2p (Figure S37A) spectra of each anode and cathode after the stability test, a slight peak shift was found due to the change in the mixed oxidation state. The Raman spectra, displayed in Figure S37B, exhibit three distinct peaks for both the cathode and anode materials. These peaks substantiate the simultaneous presence of mixed Ni$^{3+/4+}$ oxidation states and FeOOH phases. While the contributions of the NiOOH and FeOOH phases have been explored previously in NiFe catalysts, the current study primarily aims to elucidate the role of S-doped NiFe(OH)$_2$ in these reactions. Our investigation focused mainly on two types of samples: those constructed from nickel foam and those built from nickel fibrous membranes. Notably, the samples based on nickel membranes demonstrate superior overall activity, a fact attributed to advanced electrode design and potentially the presence of multiple active phases. Nevertheless, this does not detract from the pivotal role that S-doped NiFe(OH)$_2$ plays across both substrate types. A series of meticulously executed experiments confirmed that sulfur doping consistently amplifies electrocatalytic activity in both types of electrodes. This marked improvement further confirms S-doped NiFe(OH)$_2$ to be the primary active site driving the observed electrocatalytic performance. Figure 7F shows the performances of the AEM water electrolyzer with symmetric Ni–S–NiFe(OH)$_2$ electrodes at different temperatures. Notably, this symmetric configuration water electrolyzer achieves a high current density of ~2 A cm^{-2} at a cell voltage of ~1.78 V in 1 M KOH at 60°C. This configuration demonstrates enhanced performance relative to S–NiFe(OH)$_2$ electrodes (Figure S38A) and asymmetric configurations as reported in recent publications. Comparative details and the reference numbers are summarized in Table S4.[4,5,10,21,26–28,65] To further investigate the superior performance of the membrane-type Ni–S–NiFe(OH)$_2$ electrodes in AEM water electrolyzers, the detailed overvoltage analysis was conducted to investigate the specific contributions of different types of overvoltages. It is well recognized that the total overvoltage in water electrolyzer systems can be subdivided into η_{ohm}, η_{kin}, and η_{mass}.[66–69] As observed in the Nyquist plots (Figure S38B), the symmetric Ni–S–NiFe (OH)$_2$ demonstrated significantly lower R_{HFR} and R_{ct} values than its S–NiFe(OH)$_2$ counterpart, indicating the improved ion and electron transfer capabilities at the interfaces provided by the interconnected conductive fibrous matrix of the membrane-type electrodes. Furthermore, as shown in Figure S38C, the Tafel slope for Ni–S–NiFe(OH)$_2$ in the low current density region was significantly lower (203.6 mV dec^{-1}) compared to that of S–NiFe(OH)$_2$ (368.5 mV dec^{-1}), indicating superior water electrolysis kinetics. As illustrated in Figure 7G, the overvoltages for the alkaline water electrolyzer with membrane-type symmetric electrodes were significantly lower across all current density regions compared to nickel-foam-based electrodes. For instance, at a current density of 0.6 A cm^{-2}, the Ni–S–NiFe(OH)$_2$ membrane-type electrodes demonstrated a ~56% reduction in total overvoltage. This reduction is further subdivided into ~75.8% in η_{ohm}, ~44.9% in η_{kin}, and ~66.8% in η_{mass}. Figure 7H is particularly illuminating in this regard; it demonstrates that the difference in voltage between E_{kin} and the other voltages ($E_{iR-corrected}$ and E_{cell}) in the membrane-type electrode system is considerably less than that in the nickel-foam-based electrode system (Figure S39). This finding highlights not only the reduced impact of kinetic overvoltage in the membrane-type system but also its significant mitigation of performance losses due to ohmic and mass transport resistances. Lastly, as illustrated in Figure 7I, this system is capable of generating an ampere-scale current density at less than 2.0 V, even under mild conditions. This includes using a 1 M KOH electrolyte at 25°C, while maintaining consistent performance for over 140 h. This approach effectively mitigates the typical performance degradation in AEM water electrolysis systems under harsh conditions, primarily due to AEM degradation.

4 | CONCLUSIONS

In this study, a freestanding, fibrous membrane electrode was engineered specifically for AEM water electrolysis systems. Utilizing a two-step synthesis process and magnetic field alignment, the electrode displayed significant improvements in both practical performance and operational stability, which are factors crucial to industrial-scale AEM water electrolysis. Low overpotentials in both HER and OER under iR-correction-free conditions distinguished the electrode. DFT calculations supported these findings, attributing the superior bifunctional activity to the optimized Gibbs free energy on the S–NiFe(OH)$_2$ lattice. In a symmetric AEM water electrolyzer configuration, the bifunctional electrodes achieved a current density of $1\,A\,cm^{-2}$ at an applied voltage of $1.88\,V$ at room temperature, without the necessity for iR correction, highlighting the voltage of the electrode for practical utilization in AEM water electrolysis systems. Further, the electrode exhibited excellent operating stability during on–off cycles and reverse polarity tests, affirming its suitability for long-term applications. By establishing a new benchmark for practical, reversible, ampere-scale bifunctional activity, the study offers a foundation for future research and commercial opportunities in the field of AEM water electrolysis.

CONFLICT OF INTEREST STATEMENT

The authors declare that there are no conflicts of interests.

ORCID

Sung Hoon Ahn http://orcid.org/0000-0002-4971-9054

REFERENCES

1. Rocha F, Delmelle R, Georgiadis C, Proost J. Electrochemical performance enhancement of 3D printed electrodes tailored for enhanced gas evacuation during alkaline water electrolysis. *Adv Energy Mater.* 2022;13(1):2203087.
2. Chen N, Paek SY, Lee JY, et al. High-performance anion exchange membrane water electrolyzers with a current density of $7.68\,A\,cm^{-2}$ and a durability of 1000 hours. *Energy Environ Sci.* 2021;14(12):6338-6348.
3. Wan L, Xu Z, Xu Q, et al. Key components and design strategy of the membrane electrode assembly for alkaline water electrolysis. *Energy Environ Sci.* 2023;16(4):1384-1430.
4. Wei Z, Guo M, Zhang Q. Scalable electrodeposition of NiFe-based electrocatalysts with self-evolving multi-vacancies for high-performance industrial water electrolysis. *Appl Catal B.* 2023;322:122101.
5. Wang F-L, Dong Y-W, Yu C-J, et al. Trojan strategy assisted phase-pure Fe-NiCo$_2$S$_4$ for industrial anion-exchange membrane water electrolyzer. *Appl Catal B.* 2023;331:122660.
6. Kong T-H, Thangavel P, Shin S, et al. In-situ ionomer-free catalyst-coated membranes for anion exchange membrane water electrolyzers. *ACS Energy Lett.* 2023;8(11):4666-4673.
7. Wen Q, Yang K, Huang D, et al. Schottky heterojunction nanosheet array achieving high-current-density oxygen evolution for industrial water splitting electrolyzers. *Adv Energy Mater.* 2021;11(46):2102353.
8. Wu L, Ning M, Xing X, et al. Boosting oxygen evolution reaction of (Fe,Ni)OOH via defect engineering for anion exchange membrane water electrolysis under industrial conditions. *Adv Mater.* 2023;35(44):2306097.
9. Qian Q, Li Y, Liu Y, Zhang G. General anion-exchange reaction derived amorphous mixed-metal oxides hollow nanoprisms for highly efficient water oxidation electrocatalysis. *Appl Catal B.* 2020;266:118642.
10. Wang F-L, Xu N, Yu C-J, et al. Porous heterojunction of Ni$_2$P/Ni$_7$S$_6$ with high crystalline phase and superior conductivity for industrial anion exchange membrane water electrolysis. *Appl Catal B.* 2023;330:122633.
11. Wu J, Wang Z-F, Guan T, et al. Optimizing band structure of CoP nanoparticles via rich-defect carbon shell toward bifunctional electrocatalysts for overall water splitting. *Carbon Energy.* 2023;5(3):e268.
12. Lee SA, Kim J, Kwon KC, Park SH, Jang HW. Anion exchange membrane water electrolysis for sustainable large-scale hydrogen production. *Carbon Neutral.* 2022;1(1):26-48.
13. Zheng W. iR compensation for electrocatalysis studies: considerations and recommendations. *ACS Energy Lett.* 2023;8(4):1952-1958.
14. Martindale BCM, Reisner E. Bi-functional iron-only electrodes for efficient water splitting with enhanced stability through in situ electrochemical regeneration. *Adv Energy Mater.* 2016;6(6):1502095.
15. Anantharaj S, Noda S. iR drop correction in electrocatalysis: everything one needs to know! *J Mater Chem A.* 2022;10(17):9348-9354.
16. Yang F, Kim MJ, Brown M, et al. Alkaline water electrolysis at $25\,A\,cm^{-2}$ with a microfibrous flow-through electrode. *Adv Energy Mater.* 2020;10(25):2001174.
17. Xu X, Fu G, Wang Y, et al. Highly efficient all-3D-printed electrolyzer toward ultrastable water electrolysis. *Nano Lett.* 2023;23(2):629-636.
18. Han Z, Wang G, Zhang J, et al. Direct photo-curing 3D printing of nickel-based electrocatalysts for highly-efficient hydrogen evolution. *Nano Energy.* 2022;102:107615.
19. Kou T, Wang S, Shi R, et al. Periodic porous 3D electrodes mitigate gas bubble traffic during alkaline water electrolysis at high current densities. *Adv Energy Mater.* 2020;10(46):2002955.

20. Chen D, Bai H, Zhu J, et al. Multiscale hierarchical structured NiCoP enabling ampere-level water splitting for multi-scenarios green energy-to-hydrogen systems. *Adv Energy Mater*. 2023;13(22):2300499.

21. Park D-H, Kim M-H, Kim M, et al. Spherical nickel doped cobalt phosphide as an anode catalyst for oxygen evolution reaction in alkaline media: from catalysis to system. *Appl Catal B*. 2023;327:122444.

22. Feng Y, He X, Cheng M, et al. Selective adsorption behavior modulation on nickel selenide by heteroatom implantation and heterointerface construction achieves efficient co-production of H_2 and formate. *Small*. 2023;19(35):2301986.

23. Yu Z-Y, Lang C-C, Gao M-R, et al. Ni–Mo–O nanorod-derived composite catalysts for efficient alkaline water-to-hydrogen conversion via urea electrolysis. *Energy Environ Sci*. 2018;11(7):1890-1897.

24. Zhai P, Zhang Y, Wu Y, et al. Engineering active sites on hierarchical transition bimetal oxides/sulfides heterostructure array enabling robust overall water splitting. *Nat Commun*. 2020;11(1):5462.

25. Liang CW, Zou PC, Nairan A, et al. Exceptional performance of hierarchical Ni–Fe oxyhydroxide@NiFe alloy nanowire array electrocatalysts for large current density water splitting. *Energy Environ Sci*. 2020;13(1):86-95.

26. Karmakar A, Senthamaraikannan TG, Baasanjav E, et al. Surface hydroxyl group-enriched nickel cobalt molybdate hydrate for improved oxygen evolution activity in an anion exchange membrane water electrolyzer. *Appl Catal B*. 2023;328:122504.

27. Choi GH, Clament Sagaya Selvam N, Kim H, et al. High-valent metal site incorporated heterointerface catalysts for high-performance anion-exchange membrane water electrolysers. *Appl Catal B*. 2023;333:122816.

28. Zhang X-Y, Li F-T, Dong Y-W, et al. Dynamic anion regulation to construct S-doped FeOOH realizing $1000\,\text{mA}\,\text{cm}^{-2}$-level-current-density oxygen evolution over 1000 h. *Appl Catal B*. 2022;315:121571.

29. Kuai C, Xu Z, Xi C, et al. Phase segregation reversibility in mixed-metal hydroxide water oxidation catalysts. *Nat Catal*. 2020;3(9):743-753.

30. Liao H, Ni G, Tan P, et al. Oxyanion engineering suppressed iron segregation in nickel–iron catalysts toward stable water oxidation. *Adv Mater*. 2023;35(21):202300347.

31. Liu J, Du W, Guo S, et al. Iron-locked hydr(oxy)oxide catalysts via ion-compensatory reconstruction boost large-current-density water oxidation. *Adv Sci*. 2023;10(16):2300717.

32. Peng L, Yang N, Yang Y, et al. Atomic cation-vacancy engineering of NiFe-layered double hydroxides for improved activity and stability towards the oxygen evolution reaction. *Angew Chem Int Ed*. 2021;60(46):24612-24619.

33. Mehdi M, An BS, Kim H, et al. Rational design of a stable fe-rich Ni–Fe layered double hydroxide for the industrially relevant dynamic operation of alkaline water electrolyzers. *Adv Energy Mater*. 2023;13(25):2204403.

34. Kim Y, Jung S-M, Kim K-S, et al. Cathodic protection system against a reverse-current after shut-down in zero-gap alkaline water electrolysis. *JACS Au*. 2022;2(11):2491-2500.

35. Lee WH, Ko Y-J, Kim JH, et al. High crystallinity design of Ir-based catalysts drives catalytic reversibility for water electrolysis and fuel cells. *Nat Commun*. 2021;12(1):4271.

36. Balamurugan J, Nguyen TT, Aravindan V, et al. Highly reversible water splitting cell building from hierarchical 3D nickel manganese oxyphosphide nanosheets. *Nano Energy*. 2020;69:104432.

37. Yan X, Biemolt J, Zhao K, et al. A membrane-free flow electrolyzer operating at high current density using earth-abundant catalysts for water splitting. *Nat Commun*. 2021;12(1):4143.

38. Li Y, Wang W, Cheng M, et al. Arming Ru with oxygen-vacancy-enriched RuO_2 sub-nanometer skin activates superior bifunctionality for pH-universal overall water splitting. *Adv Mater*. 2023;35(24):2206351.

39. Yu L, Wu LB, McElhenny B, et al. Ultrafast room-temperature synthesis of porous S-doped Ni/Fe (oxy)hydroxide electrodes for oxygen evolution catalysis in seawater splitting. *Energy Environ Sci*. 2020;13(10):3439-3446.

40. Tan L, Yu J, Wang C, et al. Partial sulfidation strategy to NiFe-LDH@FeNi$_2$S$_4$ heterostructure enable high-performance water/seawater oxidation. *Adv Funct Mater*. 2022;32(29):2200951.

41. Lei H, Ma L, Wan Q, et al. Promoting surface reconstruction of NiFe layered double hydroxide for enhanced oxygen evolution. *Adv Energy Mater*. 2022;12(48):2202522.

42. Han X, Li N, Baik JS, et al. Sulfur mismatch substitution in layered double hydroxides as efficient oxygen electrocatalysts for flexible zinc–air batteries. *Adv Funct Mater*. 2023;33(11):2212233.

43. Muller DA, Kourkoutis LF, Murfitt M, et al. Atomic-scale chemical imaging of composition and bonding by aberration-corrected microscopy. *Science*. 2008;319(5866):1073-1076.

44. Zachman MJ, Hachtel JA, Idrobo JC, et al. Emerging electron microscopy techniques for probing functional interfaces in energy materials. *Angew Chem Int Ed*. 2020;59(4):1384-1396.

45. Zhong W, Li W, Yang C, et al. Interfacial electron rearrangement: Ni activated $Ni(OH)_2$ for efficient hydrogen evolution. *J Energy Chem*. 2021;61:236-242.

46. Lai W, Ge L, Li H, et al. In situ Raman spectroscopic study towards the growth and excellent HER catalysis of Ni/Ni $(OH)_2$ heterostructure. *Int J Hydrogen Energy*. 2021;46(53):26861-26872.

47. Mo J, Ko Y, Yun YS, et al. A carbonization/interfacial assembly-driven electroplating approach for water-splitting textile electrodes with remarkably low overpotentials and high operational stability. *Energy Environ Sci*. 2022;15(9):3815-3829.

48. Zhu W, Zhang T, Zhang Y, et al. A practical-oriented NiFe-based water-oxidation catalyst enabled by ambient redox and hydrolysis co-precipitation strategy. *Appl Catal B*. 2019;244:844-852.

49. Huang CQ, Zhou QC, Duan DS, et al. The rapid self-reconstruction of Fe-modified Ni hydroxysulfide for efficient and stable large-current-density water/seawater oxidation. *Energy Environ Sci*. 2022;15(11):4647-4658.

50. Li Y, Wu Y, Hao H, et al. In situ unraveling surface reconstruction of Ni$_5$P$_4$@FeP nanosheet array for superior alkaline oxygen evolution reaction. *Appl Catal B*. 2022;305:121033.

51. Bai L, Lee S, Hu X. Spectroscopic and electrokinetic evidence for a bifunctional mechanism of the oxygen evolution reaction. *Angew Chem Int Ed*. 2021;60(6):3095-3103.

52. Qiu Z, Tai CW, Niklasson GA, et al. Direct observation of active catalyst surface phases and the effect of dynamic

self-optimization in NiFe-layered double hydroxides for alkaline water splitting. *Energy Environ Sci*. 2019;12(2): 572-581.

53. Zhou Y-N, Yu W-L, Cao Y-N, et al. S-doped nickel-iron hydroxides synthesized by room-temperature electrochemical activation for efficient oxygen evolution. *Appl Catal B*. 2021;292:120150.

54. Li D, Wan W, Wang Z, et al. Self-derivation and surface reconstruction of Fe-doped Ni_3S_2 electrode realizing high-efficient and stable overall water and urea electrolysis. *Adv Energy Mater*. 2022;12(39):2201913.

55. Chen Y-Y, Zhang Y, Zhang X, et al. Self-templated fabrication of $MoNi_4/MoO_{3-x}$ nanorod arrays with dual active components for highly efficient hydrogen evolution. *Adv Mater*. 2017;29(39):1703311.

56. Zhao W, Xu H, Luan H, et al. NiFe layered double hydroxides grown on a corrosion-cell cathode for oxygen evolution electrocatalysis. *Adv Energy Mater*. 2022;12(2):2102372.

57. Huang Z-F, Xi S, Song J, et al. Tuning of lattice oxygen reactivity and scaling relation to construct better oxygen evolution electrocatalyst. *Nat Commun*. 2021;12(1):3992.

58. Li X, Wang Y, Wang J, et al. Sequential electrodeposition of bifunctional catalytically active structures in MoO_3/Ni-NiO composite electrocatalysts for selective hydrogen and oxygen evolution. *Adv Mater*. 2020;32(39):2003414.

59. He Y, Cui Y, Zhao Z, et al. Strategies for bubble removal in electrochemical systems. *Energy Rev*. 2023;2(1):100015.

60. Iwata R, Zhang L, Wilke KL, et al. Bubble growth and departure modes on wettable/non-wettable porous foams in alkaline water splitting. *Joule*. 2021;5(4):887-900.

61. Bae M, Kang Y, Lee DW, et al. Superaerophobic polyethyleneimine hydrogels for improving electrochemical hydrogen production by promoting bubble detachment. *Adv Energy Mater*. 2022;12(29):2201452.

62. Liu M, Min K-A, Han B, et al. Interfacing or doping? Role of Ce in highly promoted water oxidation of NiFe-layered double hydroxide. *Adv Energy Mater*. 2021;11(33):2101281.

63. Spöri C, Kwan JTH, Bonakdarpour A, et al. The stability challenges of oxygen evolving catalysts: towards a common fundamental understanding and mitigation of catalyst degradation. *Angew Chem Int Ed*. 2017;56(22):5994-6021.

64. Lee S, Cho H-S, Cho W-C, et al. Operational durability of three-dimensional Ni–Fe layered double hydroxide electrocatalyst for water oxidation. *Electrochim Acta*. 2019;315: 94-101.

65. Park YS, Liu F, Diercks D, et al. High-performance anion exchange membrane water electrolyzer enabled by highly active oxygen evolution reaction electrocatalysts: synergistic effect of doping and heterostructure. *Appl Catal B*. 2022;318:121824.

66. Wan L, Xu Z, Xu Q, et al. Overall design of novel 3D-ordered MEA with drastically enhanced mass transport for alkaline electrolyzers. *Energy Environ Sci*. 2022;15(5):1882-1892.

67. Dong S, Zhang C, Yue Z, et al. Overall design of anode with gradient ordered structure with low iridium loading for proton exchange membrane water electrolysis. *Nano Lett*. 2022; 22(23):9434-9440.

68. Babic U, Schmidt TJ, Gubler L. Communication—contribution of catalyst layer proton transport resistance to voltage loss in polymer electrolyte water electrolyzers. *J Electrochem Soc*. 2018;165(15):J3016-J3018.

69. Suermann M, Takanohashi K, Lamibrac A, Schmidt TJ, Büchi FN. Influence of operating conditions and material properties on the mass transport losses of polymer electrolyte water electrolysis. *J Electrochem Soc*. 2017;164(9):F973-F980.

SUPPORTING INFORMATION

Additional supporting information can be found online in the Supporting Information section at the end of this article.